This is an open access article published under a Creative Commons Non-Commercial No Derivative Works (CC-BY-NC-ND) Attribution License, which permits copying and redistribution of the article, and creation of adaptations, all for non-commercial purposes.

ACS Energy LETTERS

http://pubs.acs.org/journal/aelccp

LETTER

Vapour-Deposited Cesium Lead Iodide Perovskites: Microsecond Charge Carrier Lifetimes and Enhanced Photovoltaic Performance

Eline M. Hutter,*[,†] Rebecca J. Sutton,[‡] Sanjana Chandrashekar,[†] Mojtaba Abdi-Jalebi,[§] Samuel D. Stranks,[§] Henry J. Snaith,[‡] and Tom J. Savenije*[,†]

[†]Department of Chemical Engineering, Delft University of Technology, van der Maasweg 9, 2629 HZ Delft, The Netherlands

[‡]Clarendon Laboratory, University of Oxford, Parks Road, Oxford OX1 3PU, United Kingdom

[§]Cavendish Laboratory, University of Cambridge, JJ Thomson Avenue, Cambridge CB3 0HE, United Kingdom

Supporting Information

ABSTRACT: **Metal halide perovskites such as methylammonium lead iodide ($MAPbI_3$) are highly promising materials for photovoltaics. However, the relationship between the organic nature of the cation and the optoelectronic quality remains debated. In this work, we investigate the optoelectronic properties of fully inorganic vapour-deposited and spin-coated black-phase $CsPbI_3$ thin films. Using the time-resolved microwave conductivity technique, we measure charge carrier mobilities up to 25 $cm^2/(V\ s)$ and impressively long charge carrier lifetimes exceeding 10 μs for vapour-deposited $CsPbI_3$, while the carrier lifetime reaches less than 0.2 μs in the spin-coated samples. Finally, we show that these improved lifetimes result in enhanced device performance with power conversion efficiencies close to 9%. Altogether, these results suggest that the charge carrier mobility and recombination lifetime are mainly dictated by the inorganic framework rather than the organic nature of the cation.**

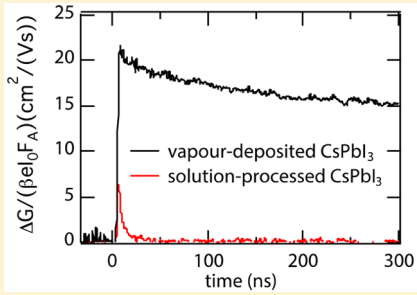

Ever since the first reports on perovskite-based solar cells,[1,2] huge efforts have been made to both improve their photovoltaic performance[3,4] and gain insight into fundamental optoelectronic properties of metal halide perovskites.[5,6] Initially, the most intensively investigated metal halide perovskite was methylammonium lead iodide ($MAPbI_3$), containing an organic cation (i.e., MA) that fills up the voids of the inorganic framework built from corner-sharing PbI_6 octahedra.[6] The rotational freedom of the dipolar organic cation has been a topic of interest[7,8] and was proposed to play a key role in properties of metal halide perovskites.[8−11] For instance, it was suggested that electron mobility is driven by dynamic disorder of the MA[9] and that metal halide perovskites owe their unique band structure to collective orientations of MA.[8,10,11] Although optoelectronic properties have been correlated with the orientation of the organic cation,[12] there is still a lack of experimental work truly revealing the interplay between the organic cation and the fundamental properties of metal halide perovskites.[13,14] To this end, replacement of MA with inorganic cesium (Cs) ions is crucial to separate the role of the cation's dipole moment from that of the lead iodide framework.[15] Although "mixed ion" perovskites comprising multiple cations can be easily made,[4,16] fully replacing the organic cation with Cs^+ is experimentally challenging because Cs-based precursors are only poorly soluble in archetypical solvents used for solution processing. Additionally, a yellow nonperovskite structure is the stable phase of $CsPbI_3$ at room temperature.[17−19] However, it was recently shown that the black perovskite phase of $CsPbI_3$ can be obtained as a metastable phase at room temperature[17,18] and that solar cells with efficiencies close to 10% can be obtained using $CsPbI_3$ produced by co-evaporation of its precursors under vacuum.[20] This improved quality of bulk $CsPbI_3$ perovskites now opens up the possibility to study their optoelectronic properties and finally enables a rational comparison to their MA-containing analogues.

In this work, we use time-resolved microwave conductivity (TRMC) measurements to investigate the charge carrier dynamics in polycrystalline $CsPbI_3$ thin films prepared using vapour deposition and different solution-based routes. Although perovskites are well-known to be easily processed

Received: July 6, 2017
Accepted: July 28, 2017
Published: July 28, 2017

 © 2017 American Chemical Society

DOI: 10.1021/acsenergylett.7b00591
ACS Energy Lett. 2017, 2, 1901−1908

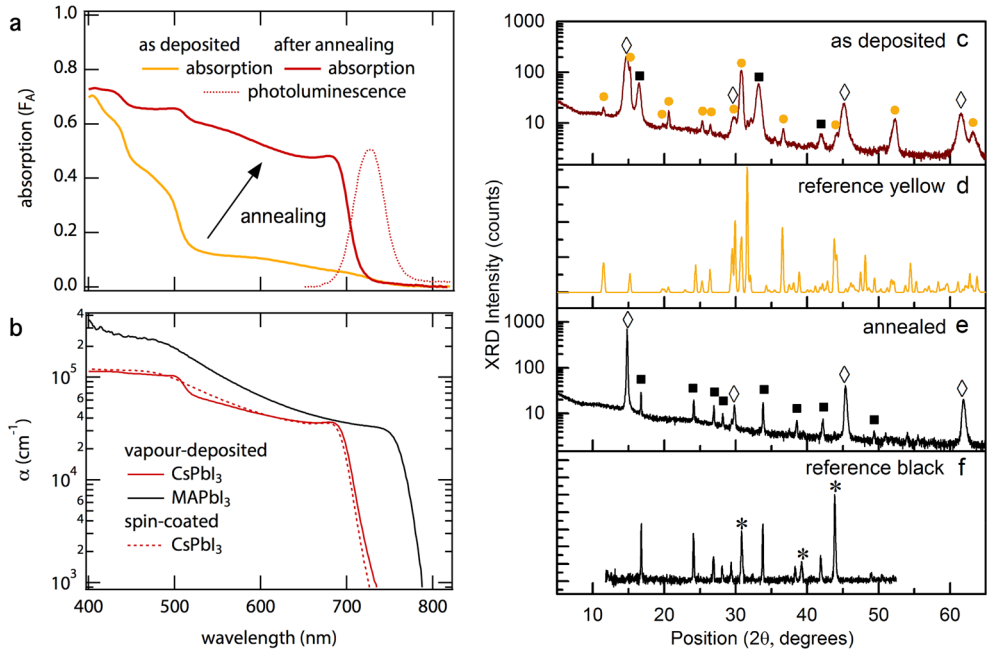

Figure 1. (a) Fraction of absorbed photons (F_A) as a function of excitation wavelength for a thin (260 nm) vapour-deposited $CsPbI_3$ film before (yellow) annealing and absorption (red, solid line) and emission spectra (red, dotted line) after annealing. (b) Wavelength-dependent absorption coefficient (red) of $CsPbI_3$, calculated using the transmission and absorption spectra for a vapour-deposited (solid line) and spin-coated (dotted line) film. The absorption coefficient of vapour-deposited $MAPbI_3$ (black line, data from ref 21) is added for comparison. (c–f) Background-subtracted X-ray (Co $\kappa\alpha$ radiation, λ = 1.79 Å) diffraction (XRD) patterns of vapour-deposited $CsPbI_3$ films before (c) and after (e) annealing, taken at room temperature using an airtight sample holder. XRD patterns of the yellow nonperovskite phase at 298 K taken from ref 28 (d) and black perovskite phase taken from ref 17 (f), both simulated for a 1.79 Å Co X-ray source. ● denotes the yellow phase, ■ denotes the black phase, ◊ denotes PbI_2, and * denotes SnO_2.

from solution, vapour deposition is an ideal method to prepare model systems of lead halide perovskites[21−23] because the film thickness can be precisely tuned and the resulting samples show reproducible quality. We find that the charge carrier mobilities in vapour-deposited polycrystalline $CsPbI_3$ films reach values around 25 $cm^2/(V\ s)$, which is very similar to values previously reported for lead iodide perovskites containing an organic cation such as MA or formamidinium (FA).[21,24,25] Furthermore, we observe impressively long charge carrier lifetimes of several μs in the vapour-deposited $CsPbI_3$ films, while both electrons and holes are immobilized within tens of ns for their spin-coated analogues. We attribute this difference to a significantly higher defect density of the latter, acting as traps to mobile charge carriers. Finally, we show that the extended charge carrier lifetimes of vapour-deposited $CsPbI_3$ result in a substantial enhancement of photovoltaic performance with respect to their spin-coated analogues.

Thin $CsPbI_3$ films of varying thicknesses were prepared using vapour deposition of its precursors. Specifically, CsI and PbI_2 powders were heated to their sublimation temperatures under vacuum (see the Experimental Methods section for more details). Although our approach is similar to previously reported co-evaporation methods,[20,22,26] we build up the $CsPbI_3$ film in a very controlled fashion by alternating the deposition of thin CsI (~2 nm) and PbI_2 (~2.5 nm) layers until the desired thickness is obtained.[21] The absorption spectrum of an as-deposited film on quartz is shown in Figure 1a. A relatively weak onset is found below 750 nm, with a steep rise in absorption at 520 nm. These results suggest that a mixture of yellow (nonperovskite) and black (perovskite) $CsPbI_3$ has formed during the deposition. That is, while its yellow phase is most stable up to 310 °C,[17] the black perovskite phase of $CsPbI_3$ is only metastable at room temperature.[18] In order to induce the yellow-to-black phase transition, the as-deposited films were annealed to 310 °C in a nitrogen-filled glovebox until these turned black. Then, the $CsPbI_3$ films were rapidly cooled to room temperature on a metal surface to "freeze" the crystals in the black phase. We note that while this black phase is highly unstable under ambient conditions, it can be maintained for at least a few days under nitrogen (see Figure S1 in the Supporting Information). Therefore, to prevent conversion back to the yellow nonperovskite phase, the samples were not exposed to air at any time before and during the optoelectronic characterization.

The red line in Figure 1a shows the absorption spectrum of the $CsPbI_3$ film after annealing, which shows a sharp onset at 730 nm, consistent with conversion to the black phase. The annealed films show an emission peak centered at 727 nm (1.71 eV); see the dotted lines in Figure 1a. Initially, the as-deposited layers are composed of relatively small grains (<50 nm), which increase in size up to a few microns upon annealing (Figure S2 in the Supporting Information). We used the absorption and transmission spectra, recorded using an integrating sphere, of the 260 nm thick $CsPbI_3$ film to determine its wavelength-dependent absorption coefficient α (see also the Experimental Methods section). The results are shown in Figure 1b, in which the α of $MAPbI_3$ (ref 14) is added for comparison. This shows that the α of $CsPbI_3$ steeply rises below 730 nm until a value of 4×10^4 cm^{-1} is reached, after which it increases gradually to 2×10^5 cm^{-1} at 400 nm. Similar to $MAPbI_3$, these values are relatively high,[27] so that thin (~300 nm) layers of $CsPbI_3$ are already sufficient to absorb most of the visible light at wavelengths shorter than the excitonic absorption peak.

DOI: 10.1021/acsenergylett.7b00591
ACS Energy Lett. 2017, 2, 1901−1908

The small absorption feature at around 500 nm hints toward the presence of either PbI_2 or yellow $CsPbI_3$ being left in the film after annealing. To further investigate the crystal structure and phase purity of the films, we measured X-ray diffraction (XRD) patterns of the films as deposited (Figure 1c) and after annealing (Figure 1e), using an airtight sample holder. The reference patterns of the yellow nonperovskite (Figure 1d)[28] and black perovskite (Figure 1f)[17] phases are added for comparison. We observe that the as-deposited film (Figure 1c) shows reflections corresponding to the black phase (denoted by squares) as well as reflections characteristic of the yellow nonperovskite phase (denoted by circles), confirming that the absorption spectrum (Figure 1a) represents a mixture of yellow and black $CsPbI_3$. After annealing, the reflections corresponding to the yellow nonperovskite phase are no longer present and the XRD pattern matches those reported in the literature (Figure 1e).[17,29] Additionally, we observe that, in general, the reflections are much broader in the as-deposited film (Figure 1c) than those after annealing (Figure 1e). This is consistent with enlargement of the crystalline domains as observed with atomic force microscopy (see Figure S1). Both before and after annealing, we observe reflections indicative of PbI_2 (diamonds) (see also Figure S3), which is most likely the origin of the absorption feature at around 500 nm in the black $CsPbI_3$ (Figure 1b).

The TRMC technique[30] was used to investigate the mobilities and recombination dynamics of photoexcited charge carriers in $CsPbI_3$ thin films frozen in the black phase. Figure 2a shows the intensity-normalized photoconductance (ΔG) of a 260 nm thick $CsPbI_3$ film, as a function of time after pulsed excitation at 600 nm. The initial rise of ΔG is attributed to the generation of mobile charges, while the decay represents their immobilization due to trapping or recombination. The product of charge carrier generation yield (φ) and the sum of their mobilities ($\sum\mu$) is obtained from the maximum signal height. In view of the low exciton binding energy of ~15 meV compared to the thermal energy at room temperature,[31] we assume that φ is close to unity. Thus, as clearly shown in Figure 2a, the sum of electron and hole mobilities in the vapour-deposited $CsPbI_3$ film is ~25 $cm^2/(V\ s)$. Interestingly, this $\varphi\sum\mu$ is very comparable to what we and others have previously measured in planar $MAPbI_3$ and $FAPbI_3$ films using similar techniques.[21,25,32] This observation suggests that the mobility in metal halide perovskites is mainly dictated by the inorganic framework rather than the nature of the monovalent cation.

As clearly visible from Figure 2a, the charge carrier lifetimes in the vapour-deposited $CsPbI_3$ (annealed) film reach values on the order of tens of microseconds at a charge carrier density of 10^{15} cm^{-3}. This is exceptionally long and only comparable to high-quality $MAPbI_3$.[33] Upon increasing the initial charge carrier density to 10^{17} cm^{-3}, the lifetime gradually decreases. This trend is characteristic for higher-order recombination between electrons and holes, for instance, second-order band-to-band recombination.[32] Upon increasing the thickness of the vapour-deposited films, both the mobility and lifetime remain constant; see Figure S4. This suggests that the optoelectronic quality of vapour-deposited polycrystalline $CsPbI_3$ films is not dependent on their thickness, which enables us to prepare electronically homogeneous layers with various thicknesses.

To investigate whether the mobilities and lifetimes observed in the vapour-deposited samples could be generalized to polycrystalline $CsPbI_3$ films, we repeated the TRMC measurements on spin-coated layers (see also XRD patterns in Figure S3). Figure 2b shows the result for a (~350 nm) film, spin-coated using a stoichiometric precursor solution in a mixture of *N*,*N*-dimethylformamide (DMF) and dimethyl sulfoxide (DMSO) and annealed to 310 °C to convert to the black phase; see the Experimental Methods for further details. We find that the mobilities in these spin-coated $CsPbI_3$ layers are close to 20 $cm^2/(V\ s)$, which is very similar to those for the vapour-deposited $CsPbI_3$ (Figure 2a). The charge carrier lifetimes, on the other hand, are significantly shorter in the spin-coated samples for equivalent excitation densities, reaching maximum values of 0.2 μs. These observations suggest that all mobile charges are rapidly immobilized in trap states, indicating

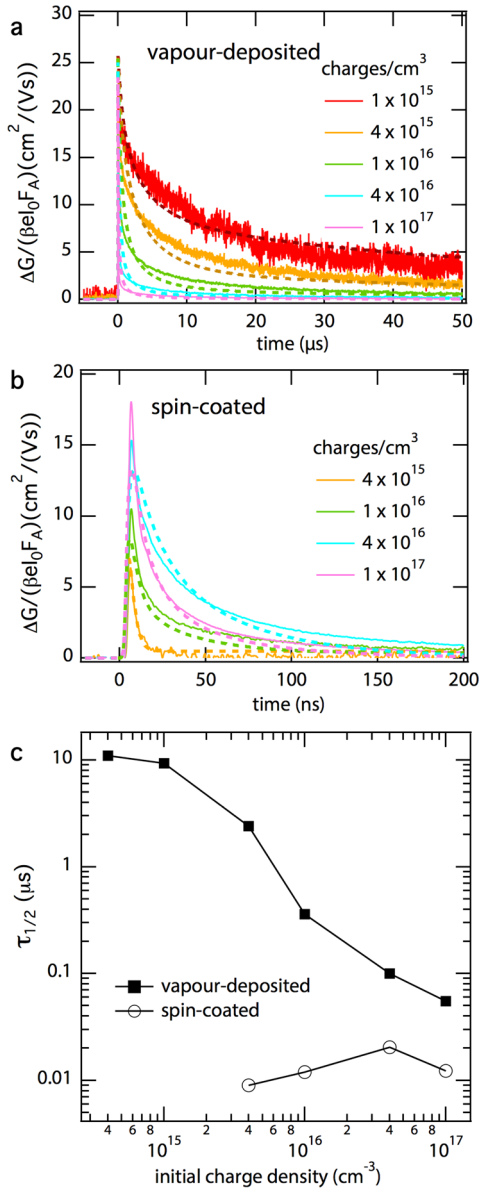

Figure 2. (a,b) TRMC traces for (a) a vapour-deposited $CsPbI_3$ thin film with thickness of 260 nm and (b) a 350 nm $CsPbI_3$ film spin-coated from a DMF/DMSO solution. Note that the horizontal time scales of (a) and (b) are different. An excitation wavelength of 600 nm was used, and the laser intensity was varied to generate initial charge carrier densities ranging from 10^{15} to 10^{17} cm^{-3}. The dotted lines are fits to the experimental data (solid lines). (c) Half lifetime as a function of the initial charge carrier density, corresponding to the $CsPbI_3$ thin films shown in (a) and (b).

DOI: 10.1021/acsenergylett.7b00591
ACS Energy Lett. 2017, 2, 1901−1908

a relatively high trap density for these type of solution-processed $CsPbI_3$ films. Most importantly, an increasing lifetime with increasing charge carrier densities is observed up to 4×10^{16} cm^{-3} (Figure 2b), while the lifetime decreases again when the number of charge carriers is further increased. We interpret this as filling of trap states until these are saturated, resulting in an enhancement of the lifetime with increasing charge carrier densities.[21]

To further visualize these observations, we have plotted the time at which the signal has reduced to half of its initial value (i.e., the half lifetime $\tau_{1/2}$) against the excitation density in Figure 2c. This clearly shows the decrease in lifetime with increasing charge densities for the vapour-deposited films (squares), which is typically observed in regimes where higher-order recombination dominates. In contrast, in the spin-coated $CsPbI_3$ (open circles), the lifetime of free charges initially increases ($<4 \times 10^{16}$ cm^{-3}), which we attribute to gradual saturation of trap states upon increasing the charge carrier density. Then, only when the latter starts exceeding the trap density ($>4 \times 10^{16}$ cm^{-3}) will higher-order recombination dominate. Considering that for the spin-coated samples free charges are rapidly immobilized into trap states, the electron and hole diffusion lengths are expected to be significantly shorter than those in the vapour-deposited films, for which long-lived free charges are generated.

In order to quantify processes such as charge carrier trapping and second order (i.e., band-to-band) recombination, we use a previously developed global kinetic model to fit the experimental TRMC data (see also Scheme S1 in the Supporting Information).[32,34] Because our measurements do not enable us to separate the contributions of electrons and holes, we initially assumed that the traps are electron-selective and that free electrons and holes have balanced mobilities based on their similar effective masses.[35] The fits are added as dotted lines in Figure 2, using the kinetic parameters listed in Table 1.

Table 1. Kinetic Parameters Used to Fit the Experimental TRMC Data Shown in Figure 2, Listing Rate Constants for Second-Order Recombination (k_2), Trap Filling (k_T), Trap Depopulation (k_D), the Trap Density (N_T), and Mobilities for Electrons (μ_e) and Holes (μ_h) for $CsPbI_3$ Thin Films Prepared via Different Routes

	vapour-deposited	spin-coated
k_2 (cm^3 s^{-1})	1.3×10^{-10}	1.2×10^{-9}
N_T (cm^{-3})	9.0×10^{14}	1.1×10^{16}
k_T (cm^3 s^{-1})	1.0×10^{-9}	6.0×10^{-8}
k_D (cm^3 s^{-1})	2.5×10^{-11}	9.0×10^{-11}
$\sum\mu$ (cm^2/(V s))	26	23

As shown in Figure 2a,b, this relatively simple kinetic model gives an excellent description of the basic features observed in the experimental decays over a wide range of excitation densities. By using a single set of kinetic parameters characteristic for each sample, we can accurately determine the rate constants for second-order recombination and trap-assisted recombination. From here, we extract that the trap densities (N_T) in the spin-coated films are on the order of 10^{16} cm^{-3}, while these are only 9×10^{14} cm^{-3} for the vapour-deposited $CsPbI_3$ layers. Furthermore, the trapping rate ($k_T = 10^{-9}$ cm^3 s^{-1}) is much higher than the trap depopulation rate ($k_D = 2.5 \times 10^{-11}$ cm^3 s^{-1}), so that at low charge carrier densities electrons get relatively rapidly trapped and subsequently slowly recombine with the free holes (see also Figure S5). At charge carrier densities above $\sim 10^{15}$ cm^{-3}, their decay is dominated by band-to-band recombination, for which we find a second-order recombination rate constant (k_2) as low as 1.3×10^{-10} cm^3 s^{-1}. From here, we conclude that the relatively long lifetimes are a combination of slow recombination of free holes with trapped electrons (at charge densities $< 10^{15}$ cm^{-3}; see also Figure S5) and slow second-order recombination between free electrons and holes (charge denisities $< 10^{17}$ cm^{-3}). Interestingly, the rate constants for both second-order recombination and trapping are on the same order of magnitude as previously reported for $MAPbI_3$,[24,32] once again suggesting that the cation actually plays a minor role in the charge carrier dynamics.

Interestingly, the experimental data for the spin-coated sample could only be fitted with the current model assuming that one of the charge carriers (for instance, the hole) is already immobilized within the instrumental response time of 3 ns. Then, its countercharge (i.e., electron) gets trapped within the time frame shown in Figure 2b (~200 ns). Therefore, it seems likely that both electrons and holes will be rapidly trapped in the spin-coated samples, which makes it challenging to collect both charges efficiently when used in a device configuration.

Finally, in line with the higher trap density in the spin-coated $CsPbI_3$ films, we find a substantial reduction in the PL emission intensity as compared to the vapour-deposited samples (see Figure S6). We note that in both cases, even at charge densities above the trap density, the external photoluminescence quantum efficiencies (PLQEs) are very low ($\ll$ 1%) and PL lifetimes are relatively short (Figure S6), which we are currently investigating.

To further investigate the relationship between the preparation route of $CsPbI_3$ and their optoelectronic quality, we constructed planar heterojunction solar cell devices in the configuration of FTO/SnO_2/$CsPbI_3$/HTM/Ag. Here, the HTM is a composite of polymer-wrapped single-walled carbon nanotubes and spiro-OMeTAD (see the Experimental Methods),[36] which enables good hole extraction without oxidation steps that require air exposure of the solar cell[37] and temporarily helps to inhibit moisture and air ingress during cell characterization in air. The results for the best-performing devices with vapour-deposited and with spin-coated $CsPbI_3$ are shown in Figure 3, and the statistics of 20 devices for each preparation route are summarized in Table 2. Consistent with their superior charge carrier lifetimes, the devices based on vapour-deposited $CsPbI_3$ (260 nm) show significantly enhanced photovoltaic performance with respect to the spin-coated layers. This results in power conversion efficiencies (PCEs) close to 9% with a highest stabilized power output (SPO) of 7.8% (see Figure 3b), which is among the highest values reported for fully inorganic perovskite-based devices.[19,38] In contrast, spin-coated $CsPbI_3$ devices gave $J-V$ measured efficiencies of up to 6.4%, which stabilized at 4.3%, which to our knowledge is already the best $J-V$ scan efficiency for devices from spin-coated polycrystalline $CsPbI_3$ thin films.[20] Higher efficiencies of up to 10% have been reported with films composed of $CsPbI_3$ nanocrystals, where suppression of the black-to-yellow phase instability occurs.[38]

The improved efficiency of the devices employing vapour-deposited $CsPbI_3$ is derived from their significantly higher values for the open-circuit voltage (V_{OC}) and fill factor (FF), which both indicate a higher-quality perovskite layer for vapour-deposited $CsPbI_3$. On average, also the short-circuit

DOI: 10.1021/acsenergylett.7b00591
ACS Energy Lett. 2017, 2, 1901−1908

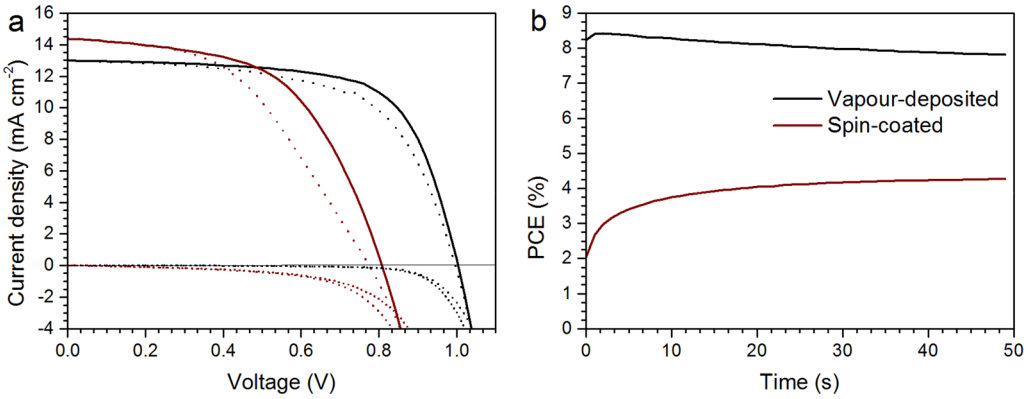

Figure 3. (a) Current−voltage (J−V) scans for the highest-efficiency spin-coated (in red) and vapour-deposited (in black) devices. Reverse scans (V_{OC} to J_{SC}) are shown with solid lines, and forward scans (J_{SC} to V_{OC}) are shown with dotted lines. Dark J−V scans are added as dotted lines. (b) SPO of PCE measurements for the same devices, measured at constant voltage.

Table 2. Statistics from J−V Data from Reverse Scans of 20 Devices from Each Preparation Method (8 devices for SPO)[a]

	vapour-deposited		spin-coated	
parameter	best cell	mean ± std. dev.	best cell	mean ± std. dev.
J_{SC} (mA cm^{-2})	13.0	12.6 ± 1.2	14.4	11.6 ± 2.6
V_{OC} (V)	1.00	0.95 ± 0.06	0.80	0.74 ± 0.13
FF	0.68	0.61 ± 0.05	0.56	0.51 ± 0.07
PCE (%)	8.80	7.27 ± 0.96	6.40	4.4 ± 1.5
SPO (%)	7.8	6.0 ± 1.3	4.3	2.5 ± 1.1
SPO ratio	0.89	0.82 ± 0.09	0.67	0.56 ± 0.14

[a]Stand. dev. is the standard deviation; SPO ratio is the ratio of the SPO with the reverse J−V scan for the same device.

current (J_{SC}) values are higher for the devices employing vapour-deposited $CsPbI_3$, even though the perovskite layers are thinner than those for the spin-coated $CsPbI_3$. These improvements are in line with the extended charge carrier lifetimes and lower trap densities observed for the vapour-deposited films (Figure 2 and Table 1). Additionally, we find that the standard deviation (20 devices from each method) for the J−V scan characteristics is substantially lower for the vapour-deposited films, which represents a significantly improved reproducibility for this method of perovskite layer deposition. When these devices are held at their maximum power point, we find the SPO is significantly closer to the J−V scan efficiency for the vapour-deposited films, which represents lower hysteresis in the device and is another indication of improved material quality.

Interestingly, the presence of PbI_2 in the vapour-deposited $CsPbI_3$ does not seem to harm its overall performance and might even turn out to be beneficial, as previously observed for $MAPbI_3$.[39] Additionally, we note that the devices were exposed to air during deposition of the electrodes and the J−V scans; therefore, these may have suffered from a slight loss of black-phase $CsPbI_3$. However, as these devices are already comparable in efficiency to $CsPbI_3$ devices in the literature,[20] our results emphasize conclusively that vapour deposition yields a higher-quality inorganic perovskite material than solution-based processing methods. In view of its optoelectronic properties, it seems likely that optimizing the device configuration and fabrication together with the quality of vapour-deposited $CsPbI_3$ itself could result in devices with much higher efficiencies. Further, given its band gap of 1.7 eV, $CsPbI_3$ is a suitable candidate to be used in tandem configuration with a Si-based bottom cell,[40] thereby having the potential to boost the efficiencies of commercially available technologies using a robust and thermally stable perovskite absorber.

To summarize, we have investigated the optoelectronic properties of fully inorganic $CsPbI_3$ perovskite thin films, prepared using vapour-deposited and solution-based methods. To freeze the $CsPbI_3$ crystals in their black perovskite phase, the films were heated to 310 °C followed by rapid cooling. Then, the charge carrier mobilities and recombination lifetimes were analyzed using the TRMC technique. We found that the mobilities are around 25 cm^2/(V s), both in vapour-deposited and spin-coated $CsPbI_3$ films. Furthermore, in vapour-deposited $CsPbI_3$, we observed lifetimes on the order of tens of microseconds, which is exceptionally long for a metal halide perovskite thin film. For the spin-coated $CsPbI_3$, we found that all free charges are immobilized within 200 ns after pulsed illumination, which we interpret as rapid trapping of electrons and holes. Upon fitting the experimental TRMC data to a previously reported kinetic model,[32,34] we extracted a trap density of 1.1×10^{16} cm^{-3} for spin-coated films and 9×10^{14} cm^{-3} for vapour-deposited $CsPbI_3$. Additionally, for the latter, we found that the rate constant for second-order recombination is 1.3×10^{-10} cm^3 s^{-1} and, hence, comparable to both MA- and $FAPbI_3$.[24,25] Importantly, these observations suggest that the organic or dipolar nature of the cation actually plays a minor role in both the mobility and band-to-band recombination of free charges in metal halide perovskites. However, in view of the somewhat higher trap densities and inferior phase stability of fully inorganic $CsPbI_3$ perovskites, the presence of MA^+ and/or FA^+ might still be crucial for these perovskites to be suitable for high-performance solar cells. On the other hand, it seems likely that postsynthetic treatments could improve the optoelectronic quality and phase stability of $CsPbI_3$.

Finally, we show that the enhanced mobilities and lifetimes in vapour-deposited $CsPbI_3$ are reflected in its performance as a photoactive layer in solar cell devices, boosting the maximum SPO from 4.3 to 7.8% (average of 2.5−6.0%). We suspect that the relatively low PCEs throughout the literature compared to $MAPbI_3$ are related to poor structural stability of black $CsPbI_3$ in combination with the limited effort on optimizing the quality of the inorganic perovskite absorber layer and devices, rather than an intrinsic limitation of fully inorganic metal halide perovskites.

DOI: 10.1021/acsenergylett.7b00591
ACS Energy Lett. 2017, 2, 1901−1908

EXPERIMENTAL METHODS

Sample Preparation. Vapour Deposition. Thin films of $CsPbI_3$ on quartz substrates were prepared by sequential physical vapour deposition of the precursors PbI_2 (≥99%, Sigma-Aldrich) and CsI (≥99.999%, Sigma-Aldrich) in a stoichiometric ratio. Therefore, an adapted evaporation machine (ATC Orion 4 - AJA International, Inc.) with a deposition controller (SQC-310 Inficon) and thermal evaporation controller (TEC-15A) was used. The PbI_2 and CsI powders were put into quartz crucibles and positioned in the vacuum chamber. After the pressure was reduced to 10^{-5}–10^{-6} mbar, the substrates (plasma-cleaned quartz for optical and structural characterization and SnO_2 on ITO glass for device fabrication) were introduced into the vacuum chamber. Then, the crucible containing the PbI_2 precursor was heated to 240–260 °C until a deposition rate of ∼0.8 Å/s was reached, as indicated by a quartz microbalance. The CsI was heated to 390–400 °C to reach a rate of ∼0.9 Å/s. $CsPbI_3$ was then obtained by alternating deposition of 2.5 nm PbI_2 and 2 nm CsI (with 5 s in between), which was repeated until the desired total thickness was reached. Finally, the films were annealed at 300 °C until these turned black. This was followed by rapid cooling on a cold metal surface.

Spin-Coating. Substrates were cleaned by sequential sonication in Hellmanex, deionized water, acetone, and isopropanol and dried with nitrogen. Immediately before spin-coating, the substrates were treated with oxygen plasma for 10 min. Solution preparation, film formation, and annealing were carried out in a nitrogen-filled glovebox. The solutions were stirred until dissolved and filtered with a 2.7 μm GF filter before spin-coating. The precursors were dissolved in a mixture of 0.65:0.35 DMF/DMSO at 0.8 M (1:1 CsI (Alfa Aesar) + PbI_2 (TCI)). Films were formed by spin-coating the precursor solution dynamically using a two-step program: 1000 rpm followed by 2000 rpm, with anisole solvent quenching after 30 s. The films were then dried at 45 °C for 10 min. The films were heated at 310–320 °C until black and cooled rapidly on a cold metal surface.

The precursors were dissolved in DMF at 0.5 M (1:1 CsI (Alfa Aesar) + PbI_2 (TCI)). Hydriodic acid was added at 35 μL per mL of solution prior to spin-coating. Films were formed by spin-coating the precursor solution dynamically using a two-step program: 1000 rpm followed by 2000 rpm. The films were then annealed at 100 °C for 10 min.

Solar Cell Device Fabrication. Fluorine-doped tin oxide (FTO)-coated glass substrates (Pilkington, 7 Ω $\square^{-1}$) were patterned using etching by 2 M HCl and Zn powder. The etched substrates were cleaned by sequential sonication in Hellmanex, deionized water, acetone, and isopropanol and dried with nitrogen. The clean substrates were then treated with oxygen plasma for 5 min before depositing the electron transport layer (ETL). The ETL was prepared by spin-coating at 3000 rpm (200 rpm/s acceleration) a solution of $SnCl_4 \cdot 5H_2O$ (0.05 M in IPA) that had been stirred for 30 min. The $SnCl_4 \cdot 5H_2O$ layer was then dried at 100 °C for 10 min and annealed at 180 °C for 60 min to form a compact layer of SnO_2. Perovskite layers were then deposited and annealed as for optical measurements. The hole transport layers (HTLs) were prepared by spin-coating 200 μL of a solution of polymer-wrapped single-walled carbon nanotubes dropwise at 3000 rpm.[36] Once dry, this was infiltrated with undoped spiro-OMeTAD by spin-coating a solution of spiro-OMeTAD (LumTec, 85 mg/mL in chlorobenzene with 33 μL/mL *tert*-butylpyridine additive) at 2000 rpm. The HTL and the active layer at the bottom of the device were removed before deposition of the bottom and top electrodes. Silver electrodes (80 nm) were deposited by thermal evaporation in an evaporator that opens to air.

Solar Cell Device Characterization. The performance of the solar cell devices was measured under simulated AM 1.5 sunlight generated with a class AAB ABET solar simulator calibrated to give simulated AM 1.5 of 100.0 mW cm^{-2} equivalent irradiance, using an NREL-calibrated KG5 filtered silicon reference cell. The mismatch factor was calculated to be 1.02 between 300 and 900 nm for $MAPbI_3$. The current–voltage curves were recorded with a sourcemeter (Keithley 2400, USA). The devices were masked with a metal aperture defining the active area (0.092 cm^2) of the device and measured in a light-tight sample holder to minimize any edge effects and to ensure that the reference cell and test cell are located during measurement in the same spot under the solar simulator. To avoid cross-talk between devices on the same substrate, the active material was removed between devices before measurement. The devices were unencapsulated and therefore exposed to ambient conditions during the measurement.

Optical Characterization. Absorption Measurements. Absorption and transmission spectra were recorded with a PerkinElmer Lambda 1050 spectrophotometer equipped with an integrated sphere. The thin films were placed in front of the sphere to measure the fraction of transmitted light (F_T) and at an angle of 10° inside of the sphere to detect the total fraction of reflected and transmitted photons (F_{R+T}). From here, we calculated the fraction of absorbed light (F_A)

$$F_A = 1 - F_{T+R} \tag{1}$$

The fraction of reflected light (F_R) was determined from

$$F_R = 1 - F_A - F_T \tag{2}$$

The absorption coefficient α is often calculated from the transmission spectrum using

$$\frac{I_L}{I_0} = e^{-\alpha L} \tag{3}$$

where I_L/I_0 equals F_T for a sample of thickness L with negligible reflection. However, because thin perovskite films are highly reflective, α was obtained from

$$\frac{F_T}{1 - F_R} = e^{-\alpha L} \tag{4}$$

Photoluminescence Quantum Efficiency (PLQE) Measurements. Perovskite films were placed in an integrating sphere and were photoexcited using a 532 nm continuous-wave laser. The laser and the emission signals were measured and quantified using a calibrated Andor iDus DU490A InGaAs detector for the determination of PL quantum efficiency. PLQE was calculated as described in ref 41.

Photoconductance Measurements. The thin films on quartz substrates were placed in an airtight microwave cell inside of an N_2-filled glovebox. The TRMC technique was used to measure the change in microwave (8.5 GHz) power after pulsed excitation (repetition rate 10 Hz) of the samples at 600 nm.[30] Neutral density filters were used to vary the intensity of the incident light. The illuminated sample area was ∼2.5 cm^2. The time-resolved change in conductance $\Delta G(t)$ was obtained from

DOI: 10.1021/acsenergylett.7b00591
ACS Energy Lett. 2017, 2, 1901–1908

the photoexcitation-induced change in microwave power $\Delta P(t)$, which are related by a sensitivity factor K

$$\frac{\Delta P(t)}{P} = -K\Delta G(t) \quad (5)$$

The rise of ΔG is limited by the width of the laser pulse (3.5 ns fwhm) and the response time of our microwave system (1 ns). The slow repetition rate of the laser of 10 Hz ensures full relaxation of all photoinduced charges to the ground state before the next laser pulse hits the sample. Before and during the photoconductance measurements, the samples were not exposed to moisture and air to prevent degradation.

■ ASSOCIATED CONTENT

Supporting Information

The Supporting Information is available free of charge on the ACS Publications website at DOI: 10.1021/acsenergylett.7b00591.

Additional absorption spectra, XRD patterns, TRMC data, atomic force microscopy images, description of the kinetic model, and photoluminescence measurements (PDF)

■ AUTHOR INFORMATION

Corresponding Authors

*E-mail: E.M.Hutter@tudelft.nl (E.M.H.).
*E-mail: T.J.Savenije@tudelft.nl (T.J.S.).

ORCID

Eline M. Hutter: 0000-0002-5537-6545
Rebecca J. Sutton: 0000-0002-6252-0840
Samuel D. Stranks: 0000-0002-8303-7292

Notes

The authors declare no competing financial interest.

■ ACKNOWLEDGMENTS

The authors thank Marcel Bus, Severin Habisreutinger, and Dharmalingam Prabhakaran for technical assistance and Amir Abbas Haghighirad for useful discussions. This work was supported by The Netherlands Organization for Scientific Research (NWO) under the Echo Grant Number 712.014.007. R.S is a Commonwealth Scholar, funded by the U.K. Government. S.D.S. received funding from the People Programme (Marie Curie Actions) of the European Union's Seventh Framework Programme (FP7/2007-2013) under REA Grant Agreement Number PIOF-GA-2013-622630. M.A.J. thanks Nava Technology Limited and Nyak Technology limited for a Ph.D. scholarship.

■ REFERENCES

(1) Kojima, A.; Teshima, K.; Shirai, Y.; Miyasaka, T. Organometal halide perovskites as visible-light sensitizers for photovoltaic cells. *J. Am. Chem. Soc.* **2009**, *131*, 6050−6051.

(2) Lee, M. M.; Teuscher, J.; Miyasaka, T.; Murakami, T. N.; Snaith, H. J. Efficient hybrid solar cells based on meso-superstructured organometal halide perovskites. *Science* **2012**, *338*, 643−647.

(3) Yang, W. S.; Park, B.-W.; Jung, E. H.; Jeon, N. J.; Kim, Y. C.; Lee, D. U.; Shin, S. S.; Seo, J.; Kim, E. K.; Noh, J. H.; et al. Iodide management in formamidinium-lead-halide−based perovskite layers for efficient solar cells. *Science* **2017**, *356*, 1376−1379.

(4) Saliba, M.; Matsui, T.; Seo, J.-Y.; Domanski, K.; Correa-Baena, J.-P.; Nazeeruddin, M. K.; Zakeeruddin, S. M.; Tress, W.; Abate, A.; Hagfeldt, A.; et al. Cesium-containing Triple Cation Perovskite Solar Cells: Improved Stability, Reproducibility and High Efficiency. *Energy Environ. Sci.* **2016**, *9*, 1989.

(5) Brenner, T. M.; Egger, D. A.; Kronik, L.; Hodes, G.; Cahen, D. Hybrid organic-inorganic perovskites: low-cost semiconductors with intriguing charge-transport properties. *Nat. Rev. Mater.* **2016**, *1*, 15007.

(6) Manser, J. S.; Christians, J. A.; Kamat, P. V. Intriguing Optoelectronic Properties of Metal Halide Perovskites. *Chem. Rev.* **2016**, *116*, 12956−13008.

(7) Gelvez-Rueda, M. C.; Cao, D. H.; Patwardhan, S.; Renaud, N.; Stoumpos, C. C.; Schatz, G. C.; Hupp, J. T.; Farha, O. K.; Savenije, T. J.; Kanatzidis, M. G.; et al. Effect of Cation Rotation on Charge Dynamics in Hybrid Lead Halide Perovskites. *J. Phys. Chem. C* **2016**, *120*, 16577−16585.

(8) Motta, C.; El-Mellouhi, F.; Kais, S.; Tabet, N.; Alharbi, F.; Sanvito, S. Revealing the role of organic cations in hybrid halide perovskite CH3NH3PbI3. *Nat. Commun.* **2015**, *6*, 7026.

(9) Ma, J.; Wang, L.-W. The nature of electron mobility in hybrid perovskite CH3NH3PbI3. *Nano Lett.* **2017**, *17*, 3646−3654.

(10) Azarhoosh, P.; McKechnie, S.; Frost, J. M.; Walsh, A.; van Schilfgaarde, M. Relativistic origin of slow electron-hole recombination in hybrid halide perovskite solar cells. *APL Mater.* **2016**, *4*, 091501.

(11) Etienne, T.; Mosconi, E.; De Angelis, F. Dynamical Origin of the Rashba Effect in Organohalide Lead Perovskites: A Key to Suppressed Carrier Recombination in Perovskite Solar Cells? *J. Phys. Chem. Lett.* **2016**, *7*, 1638−1645.

(12) Park, M.; Kornienko, N.; Reyes-Lillo, S. E.; Lai, M.; Neaton, J. B.; Yang, P.; Mathies, R. A. Critical Role of Methylammonium Librational Motion in Methylammonium Lead Iodide ($CH_3NH_3PbI_3$) Perovskite Photochemistry. *Nano Lett.* **2017**, *17*, 4151−4157.

(13) Fabini, D. H.; Labram, J. G.; Lehner, A. J.; Bechtel, J. S.; Evans, H. A.; Van Der Ven, A.; Wudl, F.; Chabinyc, M. L.; Seshadri, R. Main-Group Halide Semiconductors Derived from Perovskite: Distinguishing Chemical, Structural, and Electronic Aspects. *Inorg. Chem.* **2017**, *56*, 11−25.

(14) Hutter, E. M.; Gélvez-Rueda, M. C.; Osherov, A.; Bulović, V.; Grozema, F. C.; Stranks, S. D.; Savenije, T. J. Direct−indirect character of the bandgap in methylammonium lead iodide perovskite. *Nat. Mater.* **2016**, *16*, 115−120.

(15) Zhu, H.; Trinh, M. T.; Wang, J.; Fu, Y.; Joshi, P. P.; Miyata, K.; Jin, S.; Zhu, X. Y. Organic Cations Might Not Be Essential to the Remarkable Properties of Band Edge Carriers in Lead Halide Perovskites. *Adv. Mater.* **2017**, *29*, 1603072.

(16) McMeekin, D. P.; Sadoughi, G.; Rehman, W.; Eperon, G. E.; Saliba, M.; Horantner, M. T.; Haghighirad, A.; Sakai, N.; Korte, L.; Rech, B.; et al. A mixed-cation lead mixed-halide perovskite absorber for tandem solar cells. *Science* **2016**, *351* (6269), 151−155.

(17) Eperon, G. E.; Paterno, G. M.; Sutton, R. J.; Zampetti, A.; Haghighirad, A. A.; Cacialli, F.; Snaith, H. J. Inorganic caesium lead iodide perovskite solar cells. *J. Mater. Chem. A* **2015**, *3*, 19688−19695.

(18) Dastidar, S.; Hawley, C. J.; Dillon, A. D.; Gutierrez-Perez, A. D.; Spanier, J. E.; Fafarman, A. T. Quantitative Phase-Change Thermodynamics and Metastability of Perovskite-Phase Cesium Lead Iodide. *J. Phys. Chem. Lett.* **2017**, *8*, 1278−1282.

(19) Sutton, R. J.; Eperon, G. E.; Miranda, L.; Parrott, E. S.; Kamino, B. A.; Patel, J. B.; Hörantner, M. T.; Johnston, M. B.; Haghighirad, A. A.; Moore, D. T.; et al. Bandgap-Tunable Cesium Lead Halide Perovskites with High Thermal Stability for Efficient Solar Cells. *Adv. Energy Mater.* **2016**, *6*, 1−6.

(20) Frolova, L. A.; Anokhin, D. V.; Piryazev, A. A.; Luchkin, S. Y.; Dremova, N. N.; Stevenson, K. J.; Troshin, P. A. Highly efficient all-inorganic planar heterojunction perovskite solar cells produced by thermal coevaporation of CsI and PbI_2. *J. Phys. Chem. Lett.* **2017**, *8*, 67−72.

(21) Hutter, E. M.; Hofman, J.-J.; Petrus, M. L.; Moes, M.; Abellón, R. D.; Docampo, P.; Savenije, T. J. Charge Transfer from Methylammonium Lead Iodide Perovskite to Organic Transport Materials: Efficiencies, Transfer Rates, and Interfacial Recombination. *Adv. Energy Mater.* **2017**, *7*, 1602349.

DOI: 10.1021/acsenergylett.7b00591
ACS Energy Lett. 2017, 2, 1901−1908

(22) Liu, M.; Johnston, M. B.; Snaith, H. J. Efficient planar heterojunction perovskite solar cells by vapour deposition. *Nature* **2013**, *501*, 395−398.
(23) Momblona, C.; Gil-Escrig, L.; Bandiello, E.; Hutter, E. M.; Sessolo, M.; Lederer, K.; Blochwitz-Nimoth, J.; Bolink, H. J. Efficient vacuum deposited p-i-n and n-i-p perovskite solar cells employing doped charge transport layers. *Energy Environ. Sci.* **2016**, *9*, 3456−3463.
(24) Wehrenfennig, C.; Eperon, G. E.; Johnston, M. B.; Snaith, H. J.; Herz, L. M. High Charge Carrier Mobilities and Lifetimes in Organolead Trihalide Perovskites. *Adv. Mater.* **2014**, *26*, 1584−1589.
(25) Rehman, W.; Milot, R. L.; Eperon, G. E.; Wehrenfennig, C.; Boland, J. L.; Snaith, H. J.; Johnston, M. B.; Herz, L. M. Charge-Carrier Dynamics and Mobilities in Formamidinium Lead Mixed-Halide Perovskites. *Adv. Mater.* **2015**, *27*, 7938−7944.
(26) Momblona, C.; Gil-Escrig, L.; Bandiello, E.; Hutter, E. M.; Sessolo, M.; Lederer, K.; Blochwitz-Nimoth, J.; Bolink, H. J.; et al. Efficient vacuum deposited p-i-n and n-i-p perovskite solar cells employing doped charge transport layers. *Energy Environ. Sci.* **2016**, *9*, 3456−3463.
(27) Green, M. A.; Ho-Baillie, A.; Snaith, H. J. The emergence of perovskite solar cells. *Nat. Photonics* **2014**, *8*, 506−514.
(28) Trots, D. M.; Myagkota, S. V. High-temperature structural evolution of caesium and rubidium triiodoplumbates. *J. Phys. Chem. Solids* **2008**, *69*, 2520−2526.
(29) Ripolles, T. S.; Nishinaka, K.; Ogomi, Y.; Miyata, Y.; Hayase, S. Efficiency enhancement by changing perovskite crystal phase and adding a charge extraction interlayer in organic amine free-perovskite solar cells based on cesium. *Sol. Energy Mater. Sol. Cells* **2016**, *144*, 532−536.
(30) Savenije, T. J.; Ferguson, A. J.; Kopidakis, N.; Rumbles, G. Revealing the dynamics of charge carriers in polymer:fullerene blends using photoinduced time-resolved microwave conductivity. *J. Phys. Chem. C* **2013**, *117*, 24085−24103.
(31) Yang, Z.; Surrente, A.; Galkowski, K.; Miyata, A.; Portugall, O.; Sutton, R. J.; Haghighirad, A. A.; Snaith, H. J.; Maude, D. K.; Plochocka, P.; et al. The Impact of the Halide Cage on the Electronic Properties of Fully Inorganic Caesium Lead Halide Perovskites. *ACS Energy Lett.* **2017**, *2*, 1621−1627.
(32) Hutter, E. M.; Eperon, G. E.; Stranks, S. D.; Savenije, T. J. Charge Carriers in Planar and Meso-Structured Organic-Inorganic Perovskites: Mobilities, Lifetimes and Concentrations of Trap States. *J. Phys. Chem. Lett.* **2015**, *6*, 3082−3090.
(33) Bi, Y.; Hutter, E. M.; Fang, Y.; Dong, Q.; Huang, J.; Savenije, T. J. Charge Carrier Lifetimes Exceeding 15 μs in Methylammonium Lead Iodide Single Crystals. *J. Phys. Chem. Lett.* **2016**, *7*, 923−928.
(34) Stranks, S. D.; Burlakov, V. M.; Leijtens, T.; Ball, J. M.; Goriely, A.; Snaith, H. J. Recombination Kinetics in Organic-Inorganic Perovskites: Excitons, Free Charge, and Subgap States. *Phys. Rev. Appl.* **2014**, *2*, 34007.
(35) Amat, A.; Mosconi, E.; Ronca, E.; Quarti, C.; Umari, P.; Nazeeruddin, M. K.; Grätzel, M.; De Angelis, F. Cation-induced band-gap tuning in organohalide perovskites: Interplay of spin-orbit coupling and octahedra tilting. *Nano Lett.* **2014**, *14*, 3608−3616.
(36) Habisreutinger, S. N.; Leijtens, T.; Eperon, G. E.; Stranks, S. D.; Nicholas, R. J.; Snaith, H. J. Enhanced hole extraction in perovskite solar cells through carbon nanotubes. *J. Phys. Chem. Lett.* **2014**, *5*, 4207−4212.
(37) Abate, A.; Leijtens, T.; Pathak, S.; Teuscher, J.; Avolio, R.; Errico, M. E.; Kirkpatrik, J.; Ball, J. M.; Docampo, P.; McPherson, I.; et al. Lithium salts as "redox active" p-type dopants for organic semiconductors and their impact in solid-state dye-sensitized solar cells. *Phys. Chem. Chem. Phys.* **2013**, *15*, 2572.
(38) Swarnkar, A.; Marshall, A. R.; Sanehira, E. M.; Chernomordik, B. D.; Moore, D. T.; Christians, J. A.; Chakrabarti, T.; Luther, J. M. Quantum dot-induced phase stabilization of α-CsPbI3 perovskite for high-efficiency photovoltaics. *Science* **2016**, *354*, 92−95.
(39) Jacobsson, T. J.; Correa-Baena, J.-P.; Halvani Anaraki, E.; Philippe, B.; Stranks, S. D.; Bouduban, M. E. F.; Tress, W.; Schenk, K.; Teuscher, J.; Moser, J.-E.; et al. Unreacted PbI_2 as a Double-Edged Sword for Enhancing the Performance of Perovskite Solar Cells. *J. Am. Chem. Soc.* **2016**, *138*, 10331−10343.
(40) Beal, R. E.; Slotcavage, D. J.; Leijtens, T.; Bowring, A. R.; Belisle, R. A.; Nguyen, W. H.; Burkhard, G.; Hoke, E. T.; McGehee, M. D. Cesium lead halide perovskites with improved stability for tandem solar cells. *J. Phys. Chem. Lett.* **2016**, *7*, 746−751.
(41) de Mello, J. C.; Wittmann, H. F.; Friend, R. H. An improved experimental determination of external photoluminescence quantum efficiency. *Adv. Mater.* **1997**, *9*, 230−232.

DOI: 10.1021/acsenergylett.7b00591
ACS Energy Lett. 2017, 2, 1901−1908